Nanotechnology and Nano-Interface Controlled Electronic Devices
Editors: M. Iwamoto, K. Kaneto and S. Mashiko

CHAPTER 1

Nanostructure fabrication using electron and ion beams

Shinji Matsui

Laboratory of Advanced Science and Technology for Industry, Himeji Institute of Technology, 3-1-2 Koto, Kamigori, Ako, Hyogo, 678-1205, Japan

1. Introduction

Recent years have witnessed a number of investigations concerning nanostructure technology. The objective of research on nanostructure technology is to explore the basic physics, technology, and applications of ultra-small structures and devices with dimensions in the sub-100-nm regime. Today, the minimum size of Si and GaAs production devices is down to 0.15 μm or less. Nanostructure devices are now being fabricated in many laboratories to explore various effects, such as those created by downscaling existing devices, quantum effects in mesoscopic devices, or tunneling effects in superconductors, etc. In addition, new phenomena are being explored in an attempt to build switching devices with dimensions down to the molecular level.

Fig. 1 summarizes the resolution capabilities of several lithography processes that use electrons, ions, and photons. It includes the narrowest line width of feature size obtained with each process. Microfabrication can be classified into three regimes: submicron (1000 to 100 nm), nano (100 to 1 nm) and atom (or Ångstrom, less than 1 nm). A 256-Mb dynamic random-access memory (DRAM) Si ULSI of 0.25-μm dimensions can be fabricated by using an i-line stepper with a phase shift mask, or an excimer laser stepper. An excimer laser can be applied to a 1-Gb DRAM with 0.15 μm feature size.

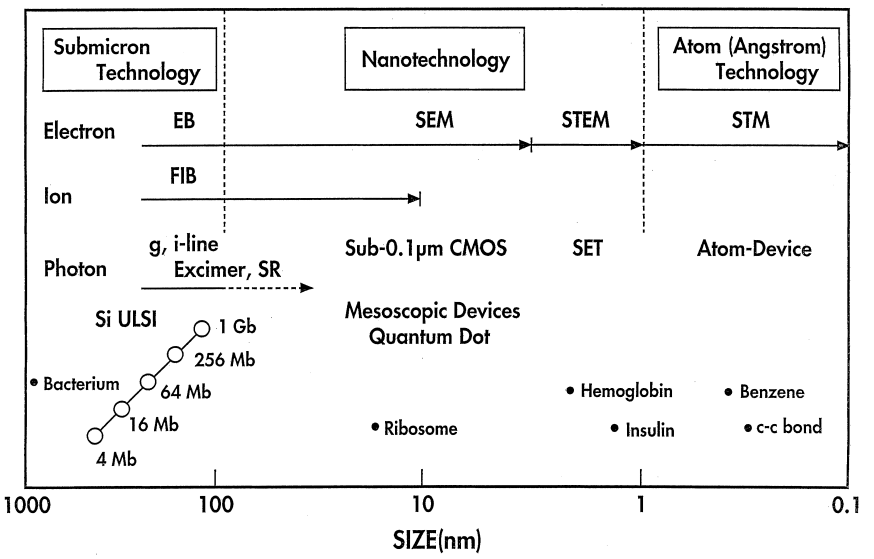

Fig. 1: Microfabrication using electrons, ions, and photons.

Electron beam (EB) lithography is the most widely used and versatile lithography tool used in fabricating nanostructure devices. Because of the availability of high-quality electron sources and optics, EB can be focused to diameters of less than 10 nm. The minimum beam diameters of scanning electron microscopes (SEM) and scanning transmission microscopes (STEM) are 1.5 and 0.5 nm, respectively. While focused-ion beam (FIB) can be focused close to 5 nm. EB and FIB can be used to make nano-scale features in the 100- to 1-nm regime. Scanning tunneling microscopy (STM) is used for atomic technology in the region of 1 to 0.1 nm.

Fig. 2 shows the resolution of various resists, which were confirmed by experiment, for electrons and ions. Minimum sizes of 8 nm for PMMA [1,2], 10 nm for ZEP (Nippon Zeopn Co.) positive resists [3], 20 nm for SAL601 (Shipley Co.) [4], and 10 nm for CALIXARENE negative resists [5] have been demonstrated using EB lithography. Nano-scale patterns have also been written in inorganic resists such as AlF_3, NaCl, and SiO_2 using STEM [6,7] and SEM [8]. Furthermore, carbon contamination patterns of 8 nm have been fabricated with SEM [9], and 8-nm PMMA patterns have been demonstrated by using Ga^+ FIB [10].

In this chapter, recent progress in nanofabrication using EB and FIB is described.

2. Electron beam nanolithography

Nanodevice fabrication requires not only high resolution but also high overlay accuracy. High-speed exposure very effectively meets the requirements because overlay accuracy is improved due to less beam drift on the nanometer scale. Moreover, it enables the use of a highly sensitive resist such as ZEP520 [11], which has sufficient resolution

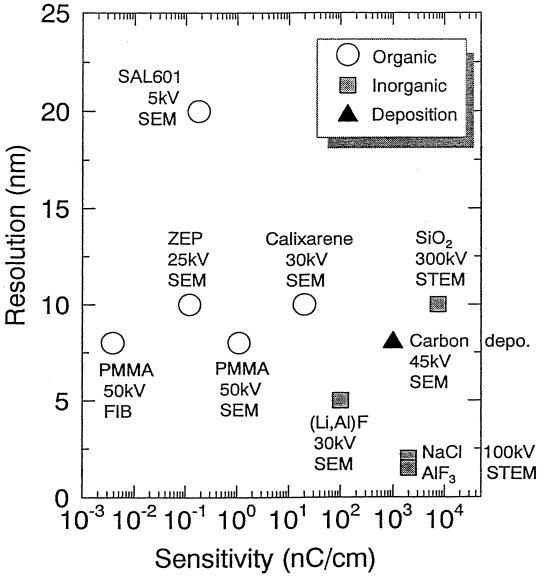

Fig. 2: Resolution of various resists for electrons and ions.

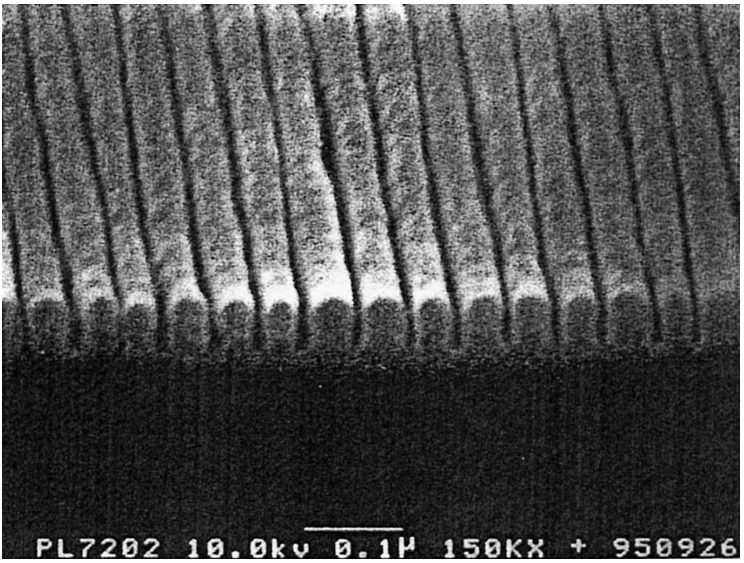

Fig. 3: 10-nm line width ZEP patterns.

and high dry etching durability for nanolithography. A 10-nm-scale resist pattern was obtained using ZEP520 positive resist. The ZEP520 resist was spin-coated onto a Si wafer to a thickness of 50 nm, and prebaked at 200°C. After EB exposure, the ZEP520 was developed with hexyl acetate for 2 min and rinsed with 2-propanol. Fig. 3 shows

a ZEP520 resist pattern in which the lines are 10 nm wide and have a pitch of 50 nm [3].

CALIXARENE is roughly a ring-shaped molecule with a diameter of about 1-nm and it works as an ultrahigh-resolution negative EB resist. CALIXARENE is a single molecule and thus is monodispersed with a molecular weight of 972. In contrast, other phenol-based resists have dispersive weights from 1000 to 100,000, which set a resolution limit. The molecular uniformity of CALIXARENE and its small molecular size is the origin of surface smoothness and the resulting ultrahigh resolution.

Such characteristics seem to be convenient for a nanodevice fabrication process. The basic component of CALIXARENE is a phenol derivative which seems to have high durability and stability, originating from the strong chemical coupling of the benzene ring. The threshold of sensitivity was about 800 μC/cm^2, which is almost 20 times higher than that of PMMA. CALIXARENE negative resist exposure was carried out. A 30-nm-thick resist was coated on a bare Si wafer. After prebaking at 170°C for 30 min, EB exposure was carried out and then the resist was developed in xylene for 20 s and was rinsed in IPA for 1 min.

The etching durability of CALIXARENE was tested using a DEM-451 (ANELVA Corp.) plasma dry-etching system with CF_4 gas. The etching rate of CALIXARENE is almost comparable with that of Si, and the durability is about four times higher than that of PMMA. This durability seems to be sufficient to make a semiconductor or a metal nanostructure.

Nanodot arrays are useful not only for quantum devices but also for studying exposure properties. In this experiment, the EB current was fixed to 100 pA at 50 kV accelerating voltage, for which the spot size is estimated to be about 5 nm. All the dot arrays were fabricated on Si substrates. And the typical exposure dose (spot dose) was about 1×10^5 electrons/dot. Fig. 4 shows typical dot array patterns having 15 nm diameter with 35 nm pitch.

Germanium pattern transfer is shown in Fig. 5. The 20-nm-thick Ge layer requires at least a 5-nm-thick CALIXARENE layer to be etched down, and the resist thickness was 30 nm. Fig. 5(a) shows the line patterns of the resist on Ge film exposed at a line dose of 20 nC/cm. Delineation was done using the S-5000 (Hitachi Corp.) SEM with a beam current of 100 pA at a 30-kV acceleration voltage. A 10-nm line width and a smooth line edge were clearly observed. This smoothness is the key point in fabricating quantum nanowires by etching processes. Fig. 5(b) shows the transferred pattern treated by 1 min of overetching, followed by oxygen-plasma treatment to remove the resist residues. A Ge line of 7 nm width was clearly observed without short cutting. Narrowing by overetching is a standard technique to obtain a fine line, however, side-wall roughness limits the line width. The smoothness of the CALIXARENE side wall enables the line width to be narrowed below the 10-nm region by overetching.

3. Room temperature nanoimprint technology

Nanoimprint-lithography (NIL) [12–18], in which resist patterns are fabricated by deforming the physical shape of the resist by embossing with a mold, is a very useful

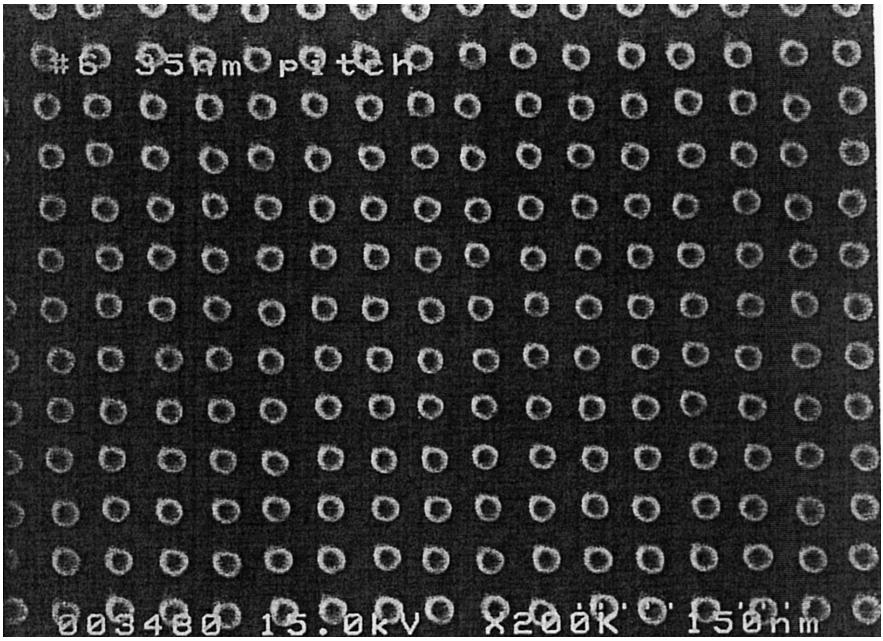

Fig. 4: CALIXARENE dot array patterns with 15 nm diameter and 35 nm pitch.

technique to make nanostructure devices; and various nanostructure devices, such as a quantized magnetic disk have, been demonstrated [19–22]. The technique has excellent features that are sub-10 nm in size over a large area and have high throughput and are low in cost.

However, a conventional NIL process has to heat a resist above the glass transition temperature to deform the physical shape of the resist with a mold. Consequently, a conventional NIL process (system) must require a thermal cycle of the resist. This heating process causes serious problems in replicated pattern accuracy, and a reduction in throughput due to the thermal cycle of the resist. In order to overcome these problems, a room temperature nanoimprint-lithography (RT-NIL) has been proposed. This RT-NIL process does not require a thermal cycle of the resist in pressing a mold onto the resist. Fig. 6 shows the difference between conventional NIL and RT-NIL. The RT-NIL process steps without heating and cooling are shorter compared with those in conventional NIL as shown in Fig. 6(a) [12,13].

First, we have demonstrated RT-NIL using Spin-on-Glass (SOG), as the material replicated and obtained excellent replicated SOG patterns and Si etched patterns by transferring replicated SOG patterns using CF_4 RIE [23]. However, SOG has the important technological shortcoming that SOG hardens gradually by reaction with water in the air at room temperature. To overcome the disadvantage, we have proposed RT-NIL using a hydrogen silsequioxane (HSQ) as the replicated material. Further, we have carried out the step-and-repeat imprinting using HSQ, and evaluated the uniformity of the replicated HSQ patterns.

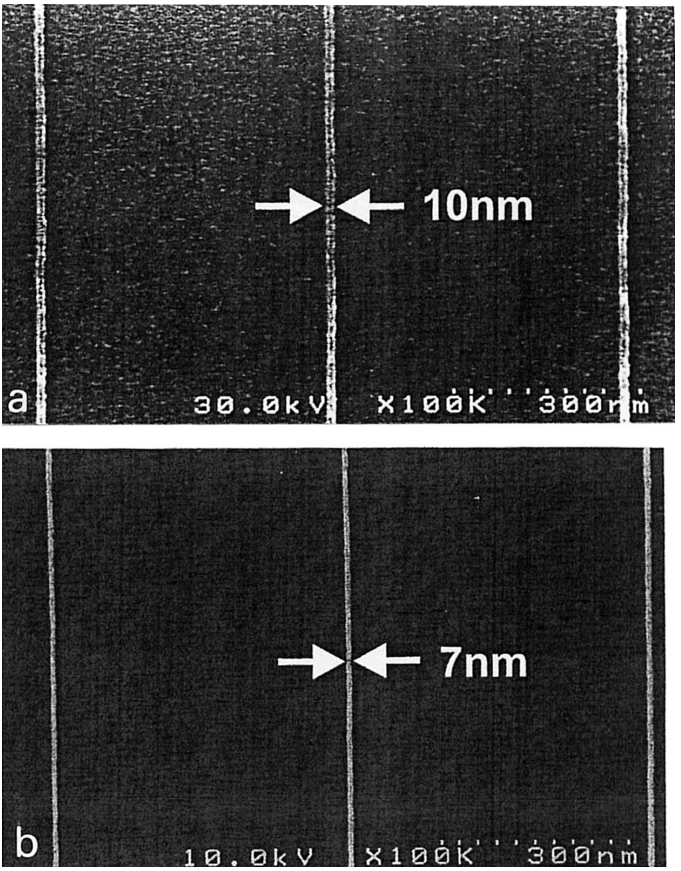

Fig. 5: Pattern transfer to Ge. (a) 10-nm line width CALIXARENE pattern and (b) transferred 7-nm line width Ge pattern.

3.1. Desktop compact imprint apparatus

The desktop compact imprint apparatus which uses a stepping motor as driving power that we have developed is shown in Fig. 7(a). The apparatus is 17 cm in width and 30 cm in height, and has 10×10 mm^2 mold-mask holder and 2 inch wafer stage. The z-positioning accuracy of the stepping motor is 2 μm per pulse. A heater is buried in the wafer stage to heat resist coated on a wafer to above the glass temperature. Therefore, by using this system, conventional NIL and RT-NIL can be performed. A 2 in. wafer can be imprinted on the x–y step-and-repeat stage. The z-axis of the mold holder and the x- and y-axis of the wafer stage are controlled by three stepping motors receiving pulse signals from a computer. The wafer temperature can be varied from room temperature up to 200°C by heating the stage, while measuring temperature with a digital thermometer. A piezo component is buried in the z axis of the mold holder to be able to measure pressures when pressing a mold-mask into the resist on the substrate.

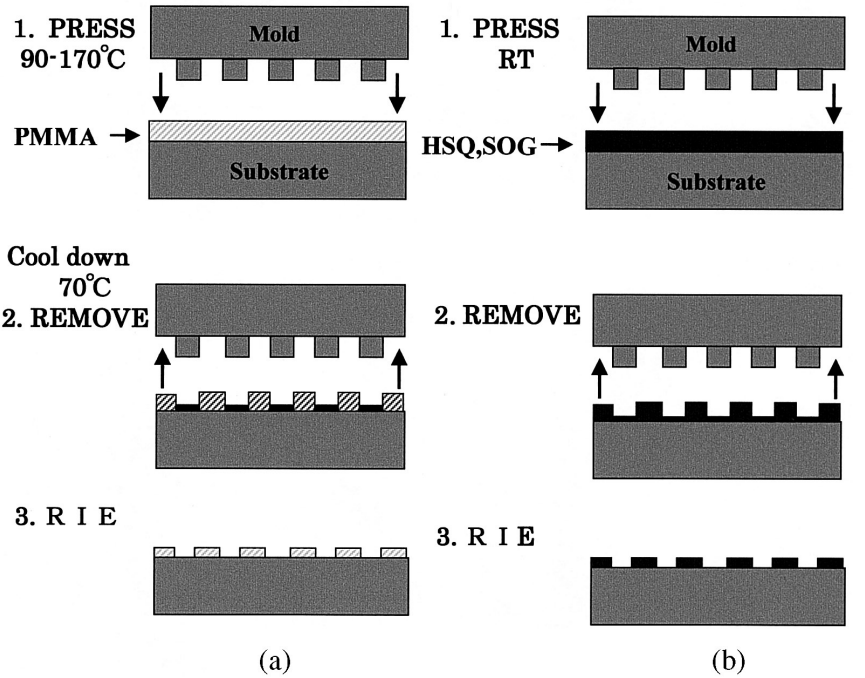

Fig. 6: Schematic of a NIL process: (a) conventional NIL using PMMA, and (b) room temperature NIL using SOG or HSQ.

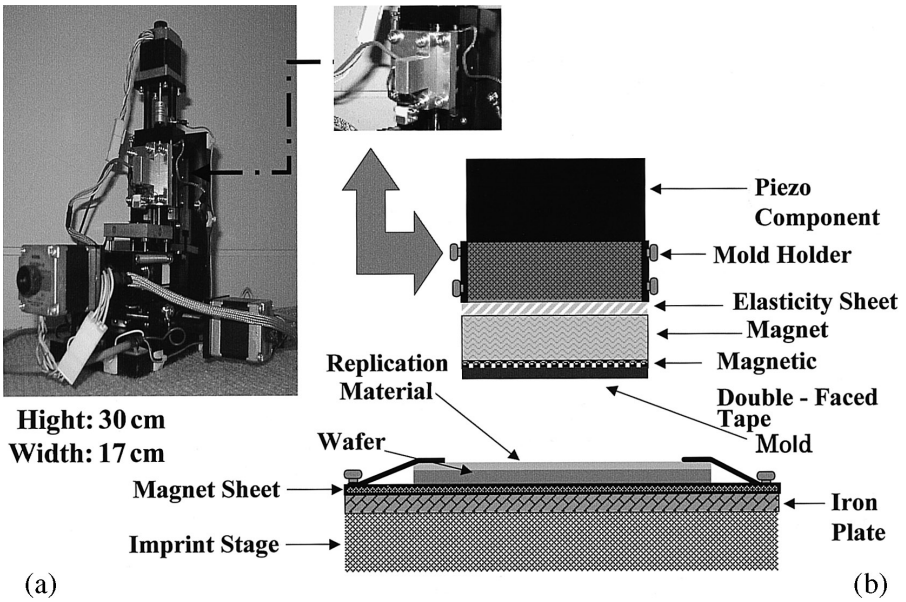

Fig. 7: (a) Desktop compact imprint system which uses a stepping motor as driving power. (b) Imprint system with a mold-mask holder and an imprint stage.

Fig. 7(b) illustrates the system of the mold-mask holder and the imprint stage. A magnet is inserted between a mold-mask and a mold wafer, and a magnetic sheet and an iron plate are inserted between the imprint stage and a wafer. The purpose of using a magnet is to make hard contact between the mold-mask and the wafer, and can bring a mold-mask into contact with a wafer in parallel in printing.

3.2. Room-temperature nanoimprint into HSQ

In this experiment, HSQ (Dow Cornig Co. FOX) which has as structure formula $H_2(SiO)_3$ was used. Infrared (IR) spectra confirmed that there was no hydrocarbon in the HSQ material. Therefore, this HSQ resin contains no organic groups, such as vinyl groups. And then, HSQ has a favorable etching durability [24]. Since HSQ has a high viscosity without pre-baking, pre-baking must be performed, in contrast to SOG, before the imprinting process. The effect of pre-baking for the HSQ is to remove the solvent from the content of HSQ, and to make the viscosity of the HSQ moderate so that physical transformation of the HSQ with a mold pattern is possible.

Fig. 8 shows the pre-baking dependence of the imprint depth when using HSQ. We measured the depth of replicated HSQ patterns with 4-μm line widths using a profiler. Imprint pressures were varied from 1.0 to 4.5 MPa. And pre-baking temperatures were varied from 50 to 200°C. The results indicate that the imprinting depth decreases suddenly around 150°C. It is suggested that the hardness of HSQ increases around 150°C. Therefore we used a pre-baking temperature in the range from 50°C to 100°C to obtain a suitable imprint depth of the replicated HSQ patterns.

An RT-NIL process using HSQ is shown Fig. 6(b). First, 0.3-μm-thick HSQ was spin-coated on an Si substrate. Then a mold and an HSQ coated substrate with pre-baking were pressed together for 1 min at a set press-pressure in the range from 2.5 to 4.5 MPa. After that, the mold was removed by the driving power of the stepping motor. Fig. 9(a), (b) and (c) show SEM photographs of a top view and at a tilt angle of 45 degrees of imprinted HSQ patterns with 0.8-μm line widths and 6-μm pitches after 1 min pressing using RT-NIL. In this experiment, an imprinting pressure of 2.0 MPa and

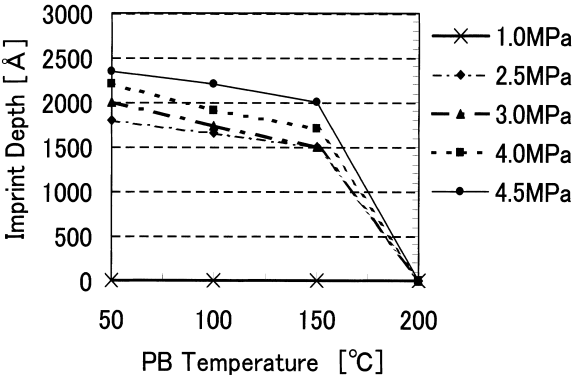

Fig. 8: Imprinting characteristics using HSQ.

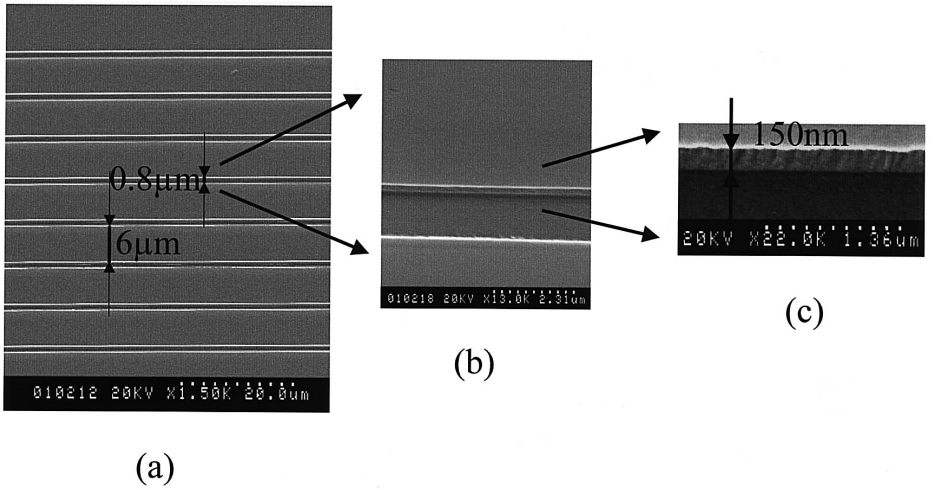

Fig. 9: SEM micrograph of (a) a top view and (b), (c) at a tilt angle of 45 degrees of imprinted HSQ patterns with 0.8-μm line widths and 6 μm pitches.

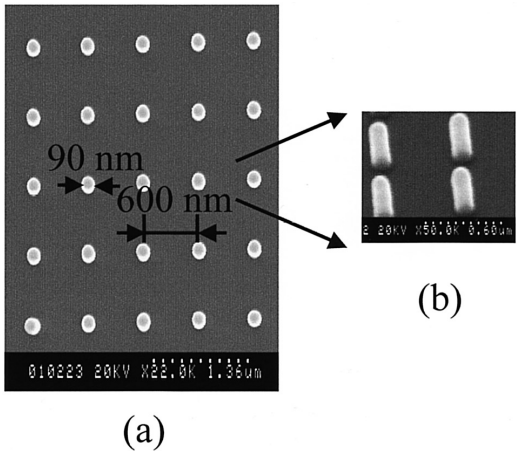

Fig. 10: SEM micrograph of (a) a top view and (b) at a tilt angle of 45 degrees of SiO_2/Si pillars mold patterns with 90 nm diameter, 600 nm period and which are 0.4 μm in height.

a pre-baking temperature of 50°C were used. It was confirmed that the imprinted depth was 150 nm and the residual depth was 150 nm from Fig. 9(c), which nearly corresponds to the imprinting characteristics using HSQ as shown in Fig. 8. Fig. 10(a) and (b) shows SEM photographs of a top view and at a tilt angle of 45 degrees of SiO_2/Si pillars mold patterns with 90 nm diameter, 600 nm period and which are 0.4 μm in height. By using the mold, holes with 90 nm diameter and 600 nm pitch were obtained after 1 min impress time by RT-NIL, as shown in Fig. 11(a) and (b). The pre-baking temperature and pressure were 60°C and 4.0 MPa. This indicates that the mold pillar patterns were

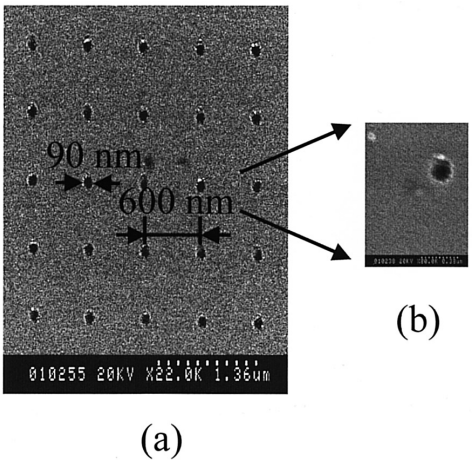

Fig. 11: SEM micrographs of a top view of holes with 90 nm diameter and 600 nm pitch imprinted after 1 min press time by RT-NIL.

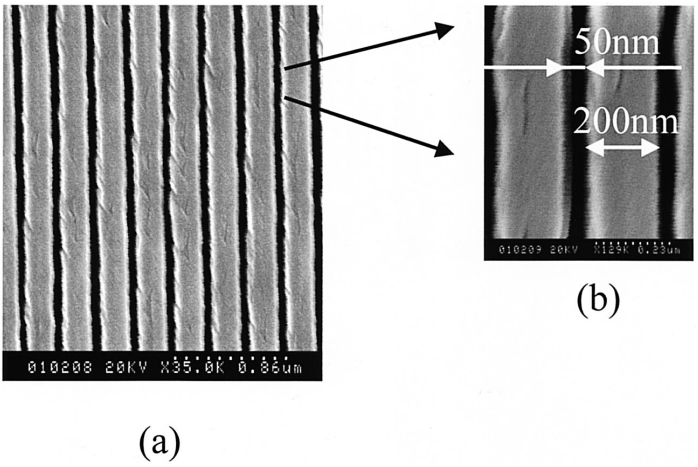

Fig. 12: SEM micrographs of patterns with 50 nm line width and 200 nm pitch replicated in HSQ using RT-NIL.

imprinted with high precision. Fig. 12 (a) and (b) show SEM photographs of patterns with 50 nm line width and 200 nm pitch replicated in HSQ using RT-NIL. These results demonstrate that RT-NIL using HSQ is a useful nanostructure fabrication technique.

4. Three-dimensional nanostructure fabrication by focused-ion-beam

Two-dimensional nanostructure fabrication using electron-beam (EB) and focused-ion-beam (FIB) has been achieved, and has been applied to make various nanostructure

devices such as single-electron transistors and MOS transistors with nanometer gate-length. Ten-nm structures can be formed by using a commercially available EB or FIB system with 5–10 nm beam diameter and a high-resolution resist [25]. Because of this, the technique of two-dimensional nanostructure fabrication is considered as established. As outlook on three-dimensional fabrication, there are three techniques using laser, EB, and FIB Chemical Vapor Deposition (CVD). Compared with three-dimensional fabrication using laser-CVD, FIB- and EB-CVD are superior [26] in the points of spatial resolution and beam-scan control. Koops et al. demonstrated some applications such as an AFM tip and field emitter by using EB-CVD [27]. Blauner et al. demonstrated pillars and walls with high aspect ratios by using FIB-CVD [28,29].

The deposition rate of FIB-CVD is much higher than that of EB-CVD due to factors such as the difference of mass between electrons and ions. Furthermore, a smaller penetration-depth of ions compared to electrons allows to make complicated three-dimensional nanostructures. For example, when we make a coil nanostructure with 100 nm line width, electrons with 10–50 keV pass the ring of the coil and reach the substrate because of the large electron range (over a few μm), so it may be difficult to make a coil nanostructure by EB-CVD. On the other hand, as the ion range is less than a few ten nm, ions stop inside the ring. So far complicated nanostructures using FIB-CVD have not been reported. This paper presents a description of the fabrication of a complicated three-dimensional nanostructure using FIB-CVD [30,31].

4.1. Fabrication process

All experiments were carried out with a commercially available FIB system (SIM9200: Seiko Instrument Inc.) utilizing a beam of 30 keV Ga^+ ions. The beam is focused to a spot size of 7 nm at 0.4 pA beam-current, and is incident perpendicularly to the surface. Phenanthrene precursor gas is evaporated from a heated container and is injected into the vacuum chamber by means of a nozzle, which is located at a height of 500 μm above the sample surface, at an angle of about 45 degrees with respect to the sample surface. The nozzle system serves to create a local high-pressure region over the surface. The base pressure of sample chamber is 2×10^{-5} Pa and the chamber pressure after introducing the source gas is 5×10^{-5} Pa. The FIB is controlled by a computer to write the desired pattern and the ion dose is adjusted to deposit a film of the desired thickness. The experiments were carried out at room temperature on a silicon substrate.

The characterization of the deposited film was performed by observation of transmission electron microscope (TEM) and measuring of Raman spectra. A carbon thin film with 200 nm thickness was deposited on a silicon substrate by 30 keV Ga^+ FIB using a phenanthrene precursor gas. The cross-section structures and electron diffraction patterns were observed by using a 300-kV TEM. The result was that there were no crystal structures in the TEM images and diffraction patterns. It is concluded that the deposited film is amorphous carbon (a-C). Raman spectra of a-C films were measured at room temperature with the 514.5 nm line of an argon ion laser. The Raman spectra were recorded by a monochromator equipped with a CCD multi-channel detector. Raman spectra were measured at 0.1–1.0 mW to avoid thermal decomposition of the samples. Fig. 13 shows Raman spectra of an a-C film deposited on a silicon substrate. A relatively

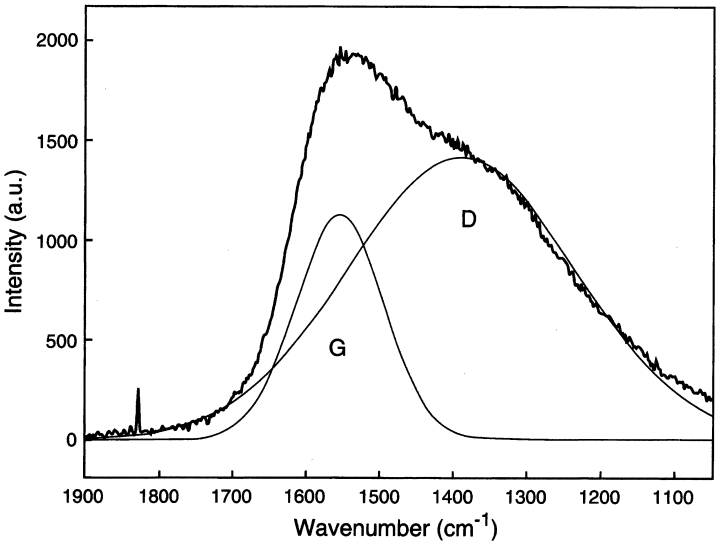

Fig. 13: Raman spectra of a diamond-like amorphous carbon film obtained at 0.1 mW by 514.4 nm excitation wavelength. The decomposed bands are shown as the G (graphite: 1550 cm^{-1}) and D (diamond: 1400 cm^{-1}) solid lines.

sharper Raman band at 1550 cm^{-1} and a broad shoulder band at around 1400 cm^{-1} are observed in the spectra excited by a 514.5 nm line. Two Raman bands were plotted after Gaussian line shape analysis. The Raman bands at 1550 cm^{-1} and 1400 cm^{-1} originate from the trigonal (sp^2) bonding structure of graphite and tetrahedral (sp^3) bond structure of diamond. This result indicates that a-C film deposited by FIB-CVD is diamond-like amorphous carbon, which has attracted attention because of the hardness, chemical inertness, and optical transparency.

The three-dimensional structure fabrication process by FIB-CVD is illustrated in Fig. 14. In FIB-CVD processes, a beam-scan is done in digital mode. First, a pillar is formed on the substrate by fixing a beam-position (position 1). After that, the beam-position is moved within the diameter of the pillar (position 2) and is then fixed until the deposited terrace thickness exceeds the ion range which is a few ten nm. This process is repeated to make three-dimensional structures. The key point to make three-dimensional structures is to adjust the beam-scan speed so that the ion-beam remains within the deposited terrace, which means that the terrace thickness exceeds an ion range. The growth conditions in the x and y directions are controlled by the beam-deflectors. The growth in the z direction is determined by the deposition rate, that is, the height of a structure is proportional to the irradiation time when the deposition rate is constant.

Figure 15 shows a branch structure made by 30 keV Ga^+ FIB-CVD. First, a pillar was made by fixing the beam-position for 120 s at 16 pA beam-current. And then, the growth of a branch was carried out using the process explained above. The diameter of the branch is 0.08 μm. The exposure time was 270 s at 0.4 pA beam-current. The experimental result indicates that arbitrary three-dimensional nanostructures can be fabricated by FIB-CVD.

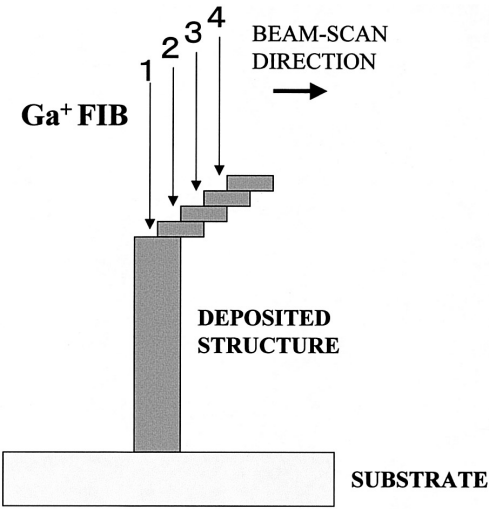

Fig. 14: Fabrication process for three-dimensional nanostructures by FIB-CVD.

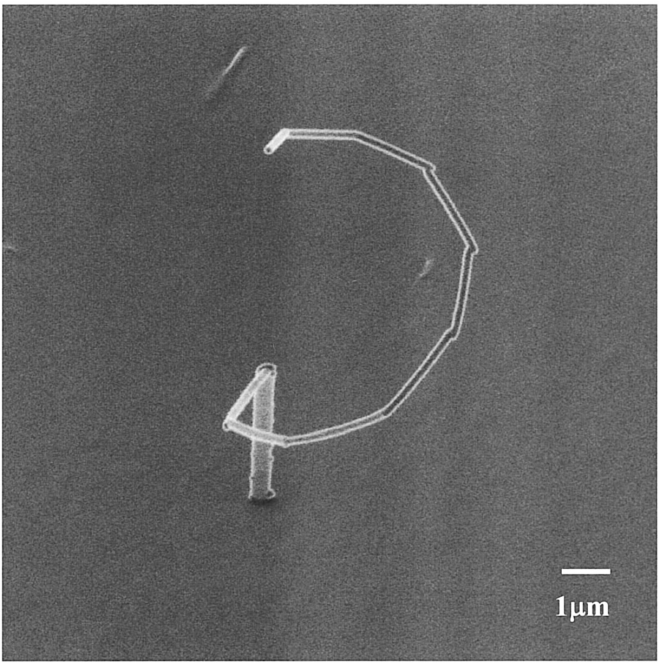

Fig. 15: Branch structure with 0.08 μm diameter.

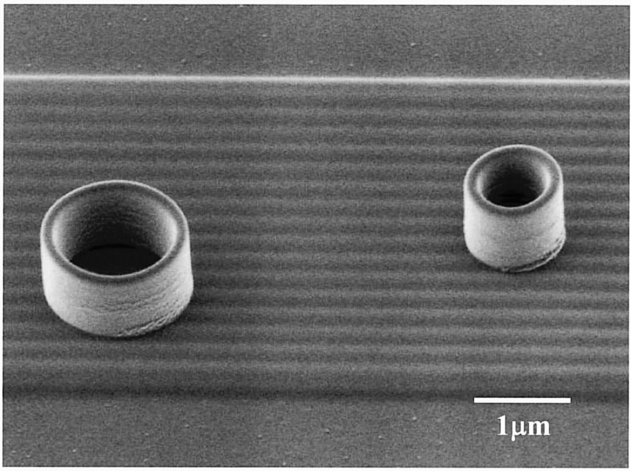

Fig. 16: Micro-beakers with 1.0 and 1.5 μm diameter, and 1.0 μm height.

4.2. Micro-system parts

Various micro-system parts were fabricated by FIB-CVD. Fig. 16 shows micro-beakers with 1.0 μm height, and 1.0 and 1.5 μm diameters. Total exposure-time of two beakers was 600 s at 16 pA beam-current. Some applications are considered, such as the study of micro-crystal growth or micro-chemical reactions by filling a beaker with the examined material.

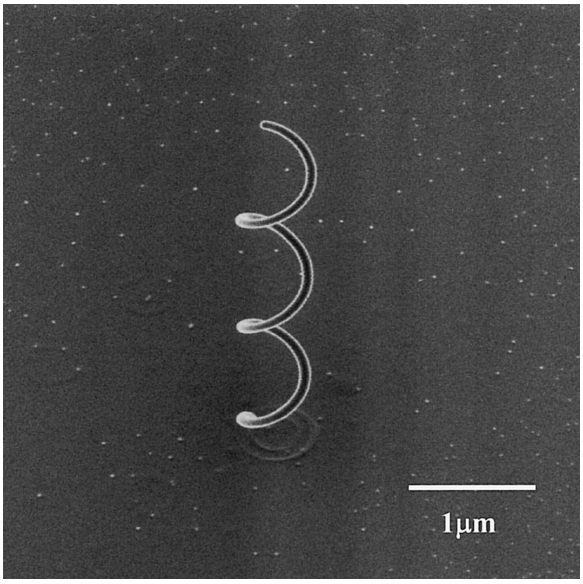

Fig. 17: Micro-coil with 0.6 μm coil-diameter, 0.7 μm coil-pitch, and 0.08 μm line width.

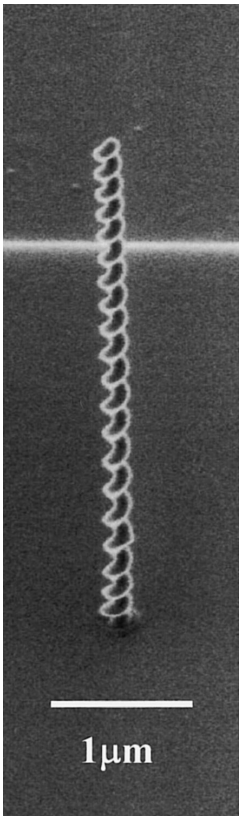

Fig. 18: Micro-drill with 0.25 μm diameter, 0.20 μm pitch, and 3.8 μm height.

Fig. 17 shows a micro-coil with 0.6 μm coil-diameter, 0.7 μm coil-pitch, and 0.08 μm line width. Exposure time was 40 s at 0.4 pA beam current. The coil-pitch can easily be changed by controlling the growth speed. Reducing the diameter of the micro-coil, a micro-drill was formed, as shown in Fig. 18. The diameter, pitch, and height of the micro-coil are 0.25, 0.20, and 3.8 μm, respectively. Exposure time was 60 s at 0.4 pA beam-current.

A bellows is one of the important parts in a mechanical system, just like a coil and a drill. Fig. 19 shows a micro-bellows with 0.8 μm pitch, 0.1 μm thickness, 2.75 μm external diameter, and 6.1 μm height. Exposure time was 300 s at 16 pA beam-current. The results show that FIB-CVD is one of the promising techniques to make parts of microsystems, although the mechanical performances of these parts have to be measured.

We intend to open up microstructure plastic arts as a new field using FIB-CVD. To demonstrate the possibility, a micro-wineglass was created as a work of microstructure plastic arts. A micro-wineglass with 2.75 μm external diameter and 12 μm height was formed on Si substrate and a human hair, as shown in Fig. 20(a) and (b). Fabrication time was 600 s at 16 pA beam-current. The beautiful micro-wineglass gives us expectations of opening up microstructure plastic arts.

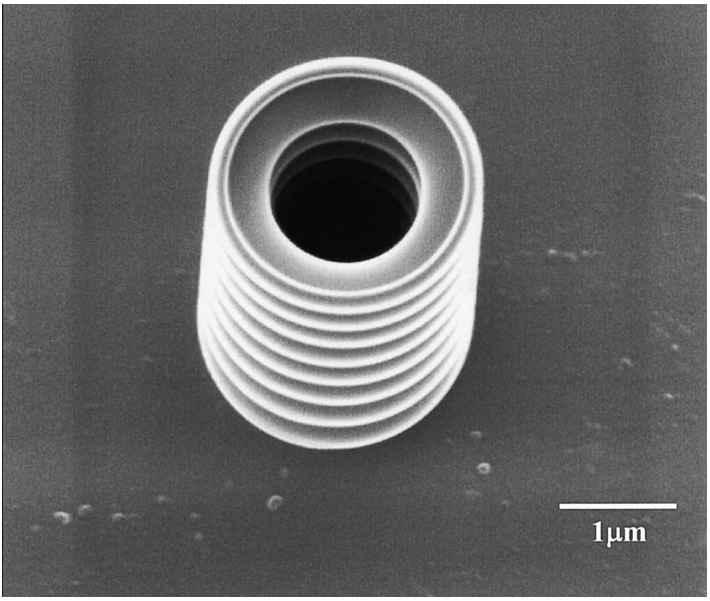

Fig. 19: Micro-bellows with 0.8 μm pitch, 0.1 μm thickness, 2.75 μm external diameter, and 6.1 μm height.

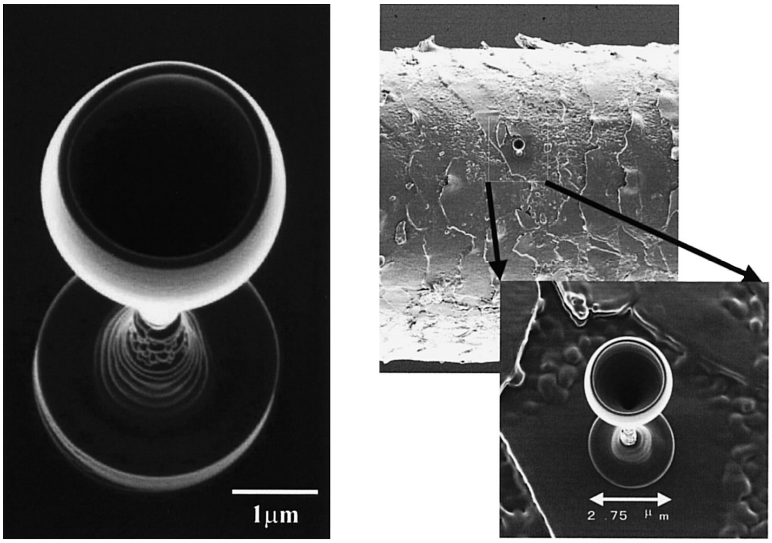

Fig. 20: Micro-wineglass with 2.75 μm external diameter and 12 μm height on (a) Si substrate and (b) human hair.

5. Summary

Ten-nanometer structure fabrication has been achieved by using a commercial available electron beam (EB) apparatus and resists. Nanoimprint lithography (NIL) is a very useful technique to overcome the low throughput and high cost in EB lithography. Room temperature NIL using HSQ as the replicated material has been proposed to achieve highly precise replication and to perform step-and-repeat imprinting. As a result, we demonstrated 50 nm line width and 90 nm in diameter hole replicated HSQ patterns, and the possibility of step-and-repeat imprinting in HSQ to 1.5 in. wafers. The results reveal that the room-temperature NIL process using HSQ as the replicated material is a very useful technique to achieve a highly precise nanoimprinting process and this technique can be applied to make nanostructure devices.

Three-dimensional structures with spatial resolution in the nanometer range can be generated with the focused-ion-beam chemical vapor deposition (FIB-CVD) technique. Three-dimensional nanostructure fabrication has been demonstrated by 30 keV Ga^+ FIB-CVD using a phenanthrene precursor. It is confirmed by TEM and Raman spectra that the deposited film is a diamond-like amorphous carbon. Micro-coil, drill, and bellows with 0.1 μm dimension were fabricated as parts of micro-systems. We propose microstructure plastic arts as a new field using micro-beam technology. A micro-wineglass with 2.75 μm external diameter and 12 μm height was created as one work. It is concluded from the experimental results that FIB-CVD direct-write processes may become interesting tools for the generation of micro- and nano-systems in the field of electronics, mechanics, optics and biology.

References

1. F. Emoto, K. Gamo, S. Namba, N. Samoto, and R. Shimizu, Jpn. J. Appl. Phys. **24**, L809 (1985).
2. W. Chen and H. Ahmed, Appl. Phys. Lett. **63**, 1116 (1993).
3. K. Kurihara, K. Iwadate, H. Namatsu, M. Nagase, H. Takenaka, and K. Murase, Jpn. J. Appl. Phys. **34**, 6940 (1995).
4. T. Yoshimura, Y. Nakayama, and S. Okazaki, J. Vac. Sci. Technol. **B10**, 2615 (1992).
5. J. Fujita, Y. Ohnishi, Y. Ochiai, and S. Matsui, Appl. Phys. Lett. **68**, 1297 (1996).
6. M. Isaacson and A. Murray, J. Vac. Sci. Technol. **19**, 1117 (1981).
7. D.R. Allee and A.N. Broers, Appl. Phys. Lett. **57**, 2271 (1990).
8. J. Fujita, H. Watanabe, Y. Ochiai, S. Manako, J.S. Tsai, and S. Matsui, Appl. Phys. Lett. **66**, 3065 (1995).
9. A.N. Broers, W.W. Molzen, J.J. Cuomo, and N.D. Wittles, Appl. Phys. Lett. **29**, 596 (1976).
10. R.L. Kubena, J.W. Ward, F.P. Stratton, R.J. Joyce, and G.M. Atkinson, J. Vac. Sci. Technol. **B9**, 3079 (1991).
11. T. Nishida, M. Notomi, R. Iga, and T. Tamamura, Jpn. J. Appl. Phys. **31**, 4508 (1992).
12. S.Y. Chou, P.R. Krauss, and P.J. Renstrom, Appl. Phys. Lett. **67**, 3114 (1995); Science **272**, 85 (1996).
13. S.Y. Chou, P.R. Krauss, W. Zhang, L. Guo, and L. Zhuang, J. Vac. Sci. Technol. **B15**, 2897 (1997).
14. X. Sun, L. Zhuang, W. Zhang, and S.Y. Chou, J. Vac. Sci. Technol. **B16**, 3922 (1998).
15. B. Heidari, I. Maximov, and L. Montelius, J. Vac. Sci. Technol. **B18**, 3557 (2000).
16. H. Schift, R.W. Jaszewski, C. David, and J. Gobrecht, Microelectronic Eng. **46**, 121 (1999).

17. T. Bailey, B.J. Choi, M. Colburn, M. Meissl, S. Shaya, J.G. Ekerdt, S.V. Sreenivasan, and C.G. Willson, J. Vac. Sci. Technol. **B18**, 3572 (2000).
18. M. Komuro, J. Taniguchi, S. Inoue, N. Kimura, Y. Tokano, H. Hiroshima, and S. Matsui, Jpn. J. Appl. Phys. **39**, 7075 (2000).
19. W. Wu, B.C.X. Sun, W. Zhang, L. Zhuang, L. Kong, and S.Y. Chou, J. Vac. Sci. Technol. **B16**, 3825 (1998).
20. L. Zhuang, L. Guo, and S.Y. Chou, Appl. Phys. Lett. **72**, 1205 (1998).
21. J. Wang, A. Schablitsky, Z. Yu, W. Wu, and S.Y. Chou, J. vac. Sci. Technol. **B17**, 2957 (1999).
22. I. Martini, S. Kuhn, M. Kamp, L. Worschech, A. Forchel, D. Eisert, J. Koeth, and R. Sijbesma, J. Vac. Sci. Technol. **B18**, 3561 (2000).
23. S. Matsui, Y. Igaku, H. Ishigaki, J. Fujita, M. Ishida, Y. Ochiai, M. Komuro, and H. Hiroshima, J. Vac. Sci. Technol. **B19**, 2801 (2001).
24. H. Namatsu, Y. Takahashi, K. Yamazaki, T. Yamaguchi, M. Nagase, and K. Kurihara, J. Vac. Sci. Technol. **B16**, 69 (1998).
25. S. Matsui, Proc. IEEE **85**, 629 (1997).
26. O. Lehmann, F. Foulon, and M. Stuke, NATO ASI Ser. E: Appl. Sci., **265**, 91–102 (1994).
27. H.W. Koops, Jpn. J. Appl. Phys. **33**, 7099 (1994).
28. A. Wargner, J.P. Levin, J.L. Mauer, P.G. Blauner, S.J. Kirch, and P. Long, J. Vac. Sci. Technol. **B8**, 1557 (1990).
29. P.G. Blauner, *Proc. 1991 Int. MicroProcess Conf.*, p. 309 (1991).
30. S. Matsui, T. Kaito, J. Fujita, M. Komuro, K. Kanda, and Y. Haruyama, J. Vac. Sci. Technol. **B18**, 3181 (2000).
31. J. Fujita, M. Ishida, T. Sakamoto, Y. ochiai, T. Kaito, and S. Matsui, J. Vac. Sci. Technol. **B19**, 2834 (2001).